



# Enhanced carbon dioxide conversion to formate on a multi-functional synergistic photoelectrocatalytic interface

Qi Shen <sup>a,1</sup>, Jun Ma <sup>a,1</sup>, Xiaofeng Huang <sup>a</sup>, Nianjun Yang <sup>b,\*</sup>, Guohua Zhao <sup>a,\*</sup>

<sup>a</sup> School of Chemical Science and Engineering, Shanghai Key Lab of Chemical Assessment and Sustainability, Tongji University, 1239 Siping Road, Shanghai 200092, China

<sup>b</sup> Institute of Materials Engineering, University of Siegen, Paul-Bonatz Str. 9-11, Siegen 57076, Germany



## ARTICLE INFO

### Article history:

Received 18 April 2017

Received in revised form 18 June 2017

Accepted 10 July 2017

Available online 11 July 2017

### Keywords:

Multi-functional interface

Synergistic photoelectrocatalysis

CO<sub>2</sub> reduction

Photonic crystal

Intrinsic Au nanoparticles

## ABSTRACT

As one of the main greenhouse gases, the conversion of CO<sub>2</sub> into useful chemicals is of great significance to global warming, climate change and energy supply. Herein, a multi-functional synergistic photoelectrocatalytic (PEC) interface is employed to realize enhanced PEC CO<sub>2</sub> reduction by using intrinsic Au doped TiO<sub>2</sub> as the light harvester, nanotube photonic crystal (NTPC) as optical channels and Cu nanoparticles (NPs) as CO<sub>2</sub> electrocatalyst. Formic acid is produced as the main product with a selectivity of 98% and a Faraday efficiency of 82.6% under simulated sunlight illumination and an applied potential of  $-1.0\text{ V}$  vs. Ag/AgCl. Its yield ratio is up to  $1019.3\text{ }\mu\text{mol L}^{-1}\text{ cm}^{-2}$  after an 8 h reduction, nearly 6.3 times higher than that on the traditional TiO<sub>2</sub> NTs. Such enhanced PEC CO<sub>2</sub> conversion performance is due to a synergistic catalytic effect on this multi-functional interface. The extraordinary localized surface plasmon resonance sensitized by the intrinsic Au NPs expands the light absorption region to the visible region. The photonic crystal layer structure raises the multi-reflection of incident light. The electrocatalyst of Cu NPs synergistically promotes PEC activity toward CO<sub>2</sub> reduction. The calculated enhancement factors of photonic crystal layer, intrinsic Au NPs, and Cu NPs are 813%, 91%, and 2028%, respectively. This work provides an effective approach for photocathode design to promote the efficiency of PEC CO<sub>2</sub> conversion.

© 2017 Elsevier B.V. All rights reserved.

## 1. Introduction

Since the industrial revolution, fossil fuel combustion has resulted in rapid increase of the atmospheric greenhouse gases levels and energy crisis. Carbon dioxide (CO<sub>2</sub>) is one of the most important greenhouse gases [1], and a nature rich C1 chemical stock as well [2]. Its conversion into high value and useful products such as CO [3], formic acid [4], methanol [5] and methane [6] and [7]. is thus beneficial to sustainable development of human society. Up to now, photoelectrocatalytic (PEC) approach has been proposed as a green and moderate approach to efficient CO<sub>2</sub> resource utilization [8,9]. It combines the merits of both electrocatalysis (EC) and photocatalysis (PC), accelerates the photo-generated electrons for directional migration and eventually improves the reduction efficiency. However, the CO<sub>2</sub> catalytic efficiency is still not satisfactory

due to the limited light absorption of semiconductor and high CO<sub>2</sub> activation reorganization energy.

Therefore, an outstanding PEC interface for CO<sub>2</sub> reduction must be a multi-functional integrated system in which light harvesting, photo-induced charge separation, CO<sub>2</sub> activation are synergistically combined [10]. Herein, a multi-functional synergistic photoelectrocatalytic interface, a nano copper decorated intrinsic Au-TiO<sub>2</sub> nanotube photonic crystal (Cu@TiO<sub>2</sub>-Au NTPC), is employed to realize enhanced PEC CO<sub>2</sub> reduction, in which intrinsic Au doped TiO<sub>2</sub> acts as the light harvester, nanotube photonic crystal (NTPC) as optical channels and Cu nanoparticles (NPs) as CO<sub>2</sub> electrocatalyst. After Inoue et al. reported for the first time about photocatalytic CO<sub>2</sub> reduction using TiO<sub>2</sub> powder [11], TiO<sub>2</sub> is still the most popular and the most investigated semiconductor photocatalyst because of its low-cost, low-toxicity, excellent UV photocatalytic activity, and chemical stability [12–17]. Nevertheless, the catalytic efficiency of CO<sub>2</sub> reduction using TiO<sub>2</sub> is still far away from satisfaction due to the limited visible light response and rapid photoelectron-hole recombination. Novel nanotechnologies have been tried to surmount these difficulties. Advanced TiO<sub>2</sub> structures have been contrived, such as bamboo-like TiO<sub>2</sub> [18], photonic crystal [19,20]. These advanced nanostructures allow the

\* Corresponding authors.

E-mail addresses: [nianjun.yang@uni-siegen.de](mailto:nianjun.yang@uni-siegen.de) (N. Yang), [g.zhao@tongji.edu.cn](mailto:g.zhao@tongji.edu.cn) (G. Zhao).

<sup>1</sup> These authors are co-first authors and contributed equally to this work.

multiple reflection of incident light, leading to an enhancement of light absorption probability. However, the absorption of light is still restricted in the UV region. On the other hand, surface plasmon resonance (SPR) of Au, Ag, and Pd nanoparticles (NPs) has been proved to enhance efficiently visible and near-infrared light absorption [21]. Through the modification of  $\text{TiO}_2$  with Au NPs, the light absorption is possible to be expanded to visible and near-infrared range [22]. For example, photocatalytic  $\text{CO}_2$  reduction and  $\text{H}_2\text{O}$  reduction under visible light irradiation have been found to be doable by use of an Au NPs/ $\text{TiO}_2$  composite [23,24]. Furthermore,  $\text{TiO}_2$  nanotubes decorated with an intrinsic Au via a self-loading process has been approved an excellent catalyst in photocatalysis [25]. In order to raise the multi-reflection of incident light and further enhance the light absorption probability, we synthesize and employ in this work intrinsic Au NPs decorated  $\text{TiO}_2$  nanotube photonic crystal ( $\text{TiO}_2$ -Au NTPC) as the photocathode.

Moreover, besides efficient light harvesting in a wide wavelength region and rapid photo-induced charge separation, an outstanding PEC interface must have the outstanding electrocatalytic properties and own a low energy barrier for  $\text{CO}_2$  activation. Of all the metals electrocatalysts, only Cu has shown a unique ability to enhance the activity and selectivity of  $\text{CO}_2$  reduction [26]. For example, the  $\text{CO}_2$  reduction products are possible to be efficiently and selectively produced via regulating the applied potentials [27]. On copper based electrocatalysts, the highest Faradaic efficiency for  $\text{CO}_2$  reduction has been realized and a wide variety of short-chained hydrocarbons (e.g., formic acid, methanol and methane) have been efficiently generated, different from those obtained on other electrocatalysts (e.g., Au, Ag and MoC) [28]. Note that, the work function of Cu is lower than the Fermi level of  $\text{TiO}_2$  [29]. When they are in contact, the band edges of  $\text{TiO}_2$  bend downward and photoinduced electrons can transfer facilely from  $\text{TiO}_2$  to Cu. Eventually, a PEC process will be driven.

Herein, we report an efficient multi-functional photocathode for synergistic PEC  $\text{CO}_2$  reduction under simulated sunlight irradiation. A novel nanomaterial,  $\text{TiO}_2$  nanotube photonic crystal structure decorated with intrinsic Au NPs is *in situ* synthesized via a simple two-step anodization on a Ti 0.2at% Au alloy foil. With unique periodic structure and SPR effect of Au NPs, the strong absorption is achieved in the UV-vis wide spectral range. To control the type and amount of reduction products, Cu NPs are decorated with the  $\text{TiO}_2$ -Au NTPC by a pulsed galvanostat method. Such a Cu@ $\text{TiO}_2$ -Au NTPC multi-functional photocathode shows excellent performance of synergistic PEC  $\text{CO}_2$  reduction. The contributions of the Au- $\text{TiO}_2$  as the light photosensitizer, NTPC as the optical channels and Cu NPs as the electrocatalyst for  $\text{CO}_2$  conversion are examined experimentally in details based on the yield ratios of reduction products at different applied potentials.

## 2. Experimental section

### 2.1. Chemicals and materials

Ti 0.2at% Au alloy foil was purchased from Northwest Institute for Non-ferrous Metal Research. Cu foil (purity 99.5%), Ethylene glycol, HF, acetone, ethanol, isopropanol, lactic acid,  $\text{CuSO}_4$ , NaOH were all analytical reagent and purchased from Sinopharm Chemical Reagent Co., Ltd., SCRC, China.

### 2.2. Synthesis of the multi-functional photocathode

The procedure employed to synthesize the Cu@ $\text{TiO}_2$ -Au NTPC photocathode is schematically shown in Scheme S1 in the Electronic Supplementary Information (ESI). First, a simplified two-step electrochemical anodization of the Ti 0.2at% Au alloy foil was con-

ducted in an ethylene glycol solution containing 0.2 M HF and 1 M  $\text{H}_2\text{O}$  to fabricate the hierarchical  $\text{TiO}_2$ -Au nanotube photonic crystal ( $\text{TiO}_2$ -Au NTPC) [25]. Prior to anodization, the alloy foil was mechanically polished with different sandpapers until a mirror-like surface was obtained. It was then degreased successively in an ultrasonic bath with acetone, ethanol, isopropanol, and deionized water. After drying with nitrogen gas, it was oxidized (namely an anodization process) using a conventional two-electrode system where a direct current (DC) power supply was applied, the alloy foil acted as the working anode, and a platinum foil behaved as the counter electrode. The first-step anodization led to the growth of a layer of  $\text{TiO}_2$  nanotubes. The optimized conditions were: a temperature of 10 °C, an applied voltage of 120 V and a reaction time of 3 h. After ultrasonically removing the as-grown nanotubes in deionized water, the second-step anodization process was applied with a voltage of 120 V for 10 min. After that, the sample was rinsed with deionized water, dried in a nitrogen stream, and further annealed at 450 °C in air for 60 min. The  $\text{TiO}_2$ -Au NTPC electrode was finally obtained after a fully crystallized process. The deposition of Cu NPs onto the  $\text{TiO}_2$ -Au NTPC was conducted at room temperature through a pulsed galvanostat method. The electrolyte was a mixture of 3 M lactic acid and 0.4 M  $\text{CuSO}_4$  [28]. Its pH was adjusted to 7 with NaOH. The optimized parameters were: a negative current pulse time of 1 s, a delay time of 7 s, a constant current density of 40 mA cm<sup>-2</sup>. In order to obtain a uniform deposition of Cu NPs into the nanotubes, the pulse cycles performed at 10, 15 and 20 cycles were investigated. According the SEM morphology and amperometric i-t characterization (Fig. S2 and Fig. S3), nanotubes loaded with Cu NPs by 15 cycles of pulsed electrodeposition were chosen as the optimum photocathode.

For comparison,  $\text{TiO}_2$  NTs was growth at 20 °C by an anodization voltage of 20 V and a reaction time of 10 min. The electrolytes included ethylene glycol with 1 vol%  $\text{H}_2\text{O}$  and 0.25 wt%  $\text{NH}_4\text{F}$ . The  $\text{TiO}_2$  NTPCs were grown by a two-step electrochemical anodization in the same electrolyte as that to synthesize  $\text{TiO}_2$  NTs. The time of the first-step and the second-step anodization process was 3 h and 10 min, respectively. After the anodization process, the samples were rinsed with ethanol and dried in a nitrogen stream, followed by a heat-treating at 500 °C for 3 h in oxygen stream.

### 2.3. Characterization

Field-emission scanning electron microscopy (FE-SEM, Hitachi S-4800, Japan) and transmission electron microscopy (TEM, JEM-2100, JEOL, Japan) were employed to characterize the morphologies of the as-prepared samples. Their crystalline structures were determined by X-ray diffractometer (XRD, Focus D8, Bruker, Germany) equipped with a Cu K $\alpha$  radiation ( $\lambda = 0.1542$  nm). The surface elements of synthesized samples were analyzed using X-ray photoelectron spectroscopy (XPS, AXIS Ultra HSA, Kratos Analytical Ltd., UK). Their optical absorption spectra were recorded as well with the UV-vis diffuse reflection spectroscopy (UV-vis DRS, Ava light-DHS, Avantes, Netherlands).

All PEC measurements were performed on a CHI 660C electrochemical workstation with a conventional three-electrode system (light Source: LA-410UV with UV cutoff, Hayashi, Japan). A platinum foil and a saturated calomel electrode (SCE) acted as the counter electrode and reference electrode, respectively. The prepared photocathodes were used as the working electrodes. In most cases, the electrolyte was 0.1 M  $\text{Na}_2\text{SO}_4$  aqueous solution. Prior to photoelectrochemical experiments, high purity  $\text{CO}_2$  (99.99%) gas stream (at a flow rate of 10 mL min<sup>-1</sup> for at least 20 min) was bubbled into the electrolyte solution to obtain  $\text{CO}_2$ -saturated solution as well as to remove dissolved oxygen from the solution. To avoid the oxidation of Cu NPs, linear sweep voltammetry (LSV) was carried out in the negative potential range (e.g., from 0.0 to -1.0 V) with a scan rate

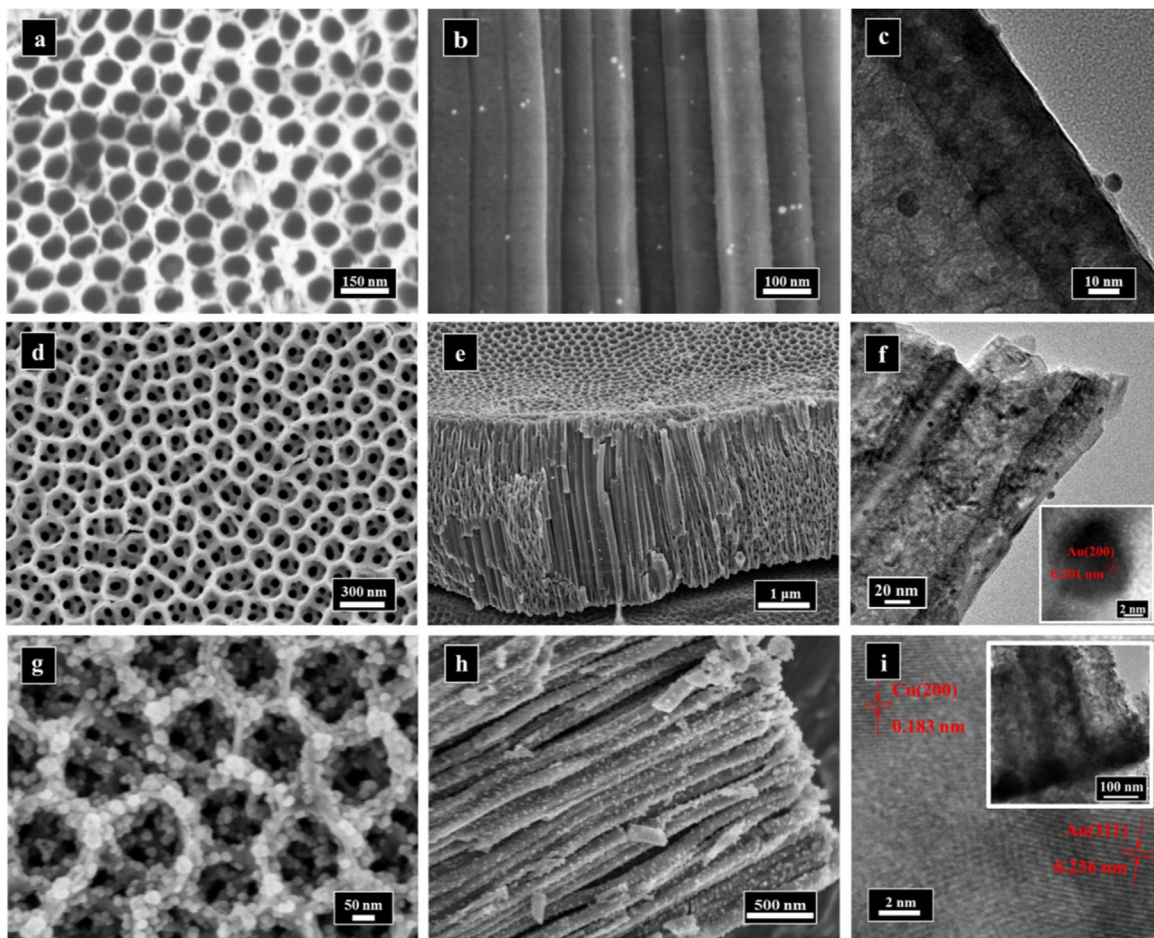


**Fig. 1.** SEM images of  $\text{TiO}_2$ -Au NTs (a, b),  $\text{TiO}_2$ -Au NTPC (d, e) and  $\text{Cu}@\text{TiO}_2$ -Au NTPC (g, h) in a top-view and side view; (c) TEM image of  $\text{TiO}_2$ -Au NTs, (f) TEM image of  $\text{TiO}_2$ -Au NTPC and the inset shows the HRTEM image of Au NPs; (i) HRTEM images of  $\text{Cu}@\text{TiO}_2$ -Au NTPC and the inset shows TEM of  $\text{Cu}@\text{TiO}_2$ -Au NTPC.

of  $50 \text{ mV s}^{-1}$ . The amperometric i-t curves were recorded at a constant potential of  $-0.7 \text{ V}$  vs. SCE. The effect of light irradiation on the photocurrent was investigated with a regular interval of 100 s for light on/off.

#### 2.4. PEC $\text{CO}_2$ reduction and product analysis

PEC  $\text{CO}_2$  reduction was conducted in a homemade gastight double-chamber with 100 mL 0.1 M  $\text{NaHCO}_3$  as the electrolyte solution. The solution was purged with high purity  $\text{CO}_2$  (99.99%) gas stream for at least 30 min at a flow rate of  $20 \text{ mL min}^{-1}$  to ensure that the dissolved oxygen was completely removed and the electrolyte solution was saturated with  $\text{CO}_2$ . The reaction was performed on a potentiostat using a three-electrode system with the as-prepared electrode as the working electrode, a graphite electrode as the counter electrode and an  $\text{Ag}/\text{AgCl}$  electrode as the reference electrode. A 300 W short-arc xenon lamp (Microsolar 300, Beijing Perfect Light Co., Ltd., China) was used as the light source. The light intensity was calibrated to the simulated sunlight patterns ( $100 \text{ mW cm}^{-2}$ ) via using an AM 1.5G optical filter.

The reduction products in the aqueous phase were determined by Nash reagent method [30]. First, 0.5 mL sample solution was added into a test tube and washed by aqua regia. 50 mg magnesium powder was added into the sample solution as well. In an ice bath, 0.5 mL 37% concentrated hydrochloric acid was dropwisely added into the mixture within 10 min. Then the pH of the mixture was neutralized with 3 mL 1 M  $\text{NaOH}$  solution. Afterwards, the mixture was centrifuged for 5 min, followed by mixing 2 mL super-

natant with 2 mL Nash reagent (25g ammonium acetate, 2.1 mL glacial acetic acid and 0.2 mL acetylacetone, dissolved in the ultra-pure water of 100 mL). Finally, the mixture was shaken for about 1 h to complete the reaction [31]. The quantification for formic acid was analysed by the Agilent 8453UV-vis spectroscopy. The absorbance detected at 413 nm was used for constructing the calibration curve. For the detection of formaldehyde, 2 mL liquid product was directly mixed with 2 mL Nash reagent. After shaking for about 1 h, the final mixture was also analysed using Agilent 8453UV-vis spectroscopy with the calibration curve established with the absorbance peak at 413 nm. The calibration curves of both formic acid and formaldehyde are shown in Fig. S1. The detection of methanol was performed using the Varian CP3900 gas chromatograph equipped with a flame ionization detector. The products in the gas phase were determined by the Techcomp GC7000 gas chromatograph equipped with a thermal couple detector.

### 3. Results and discussion

As schematically shown in Scheme S1, the  $\text{Cu}@\text{TiO}_2$ -Au NTPC photocathode is *in situ* synthesized on a Ti-Au alloy foil via a simple two-step anodization. Fig. 1 shows the samples prepared in different steps. First,  $\text{TiO}_2$ -Au nanotubes arrays ( $\text{TiO}_2$ -Au NTs) are obtained with an anodization time of 3 h. Fig. 1a and b shows SEM images of the  $\text{TiO}_2$ -Au NTs in the top view and side view, respectively. Well-aligned and one-dimensional nanotube arrays are formed on the alloy substrate. Their average diameter is about 150 nm and their wall thickness is about 30 nm. One can clearly see

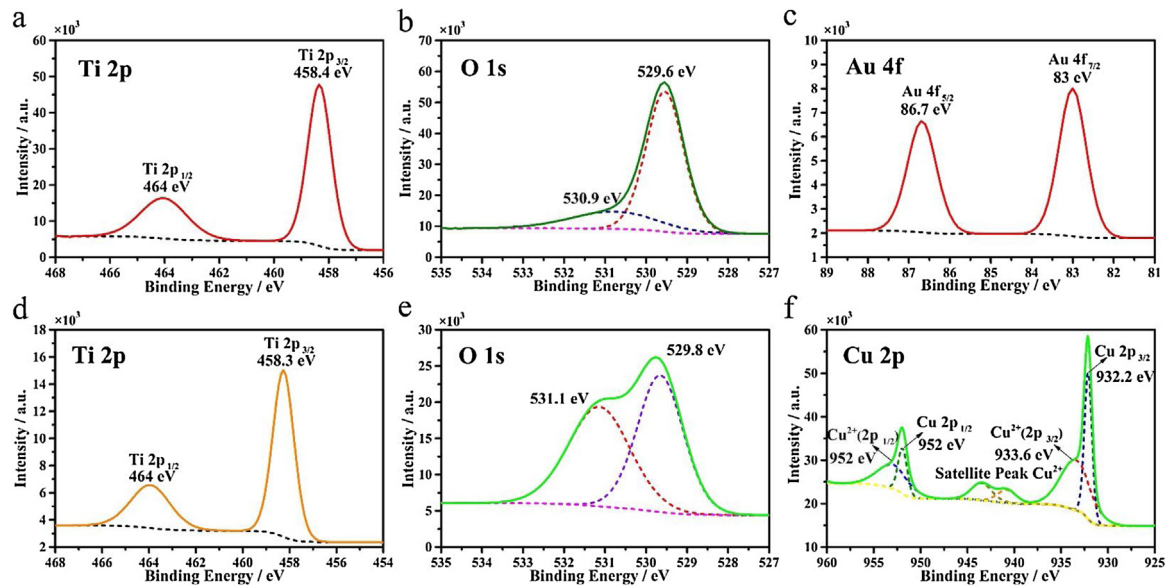


**Fig. 2.** XPS spectra of  $\text{TiO}_2$ -Au NTPC for (a) Ti 2p, (b) O 1s, (c) Au 4f as well as Cu@ $\text{TiO}_2$ -Au NTPC for (d) Ti 2p, (e) O 1s, (f) Cu 2p. The solid and dashed lines are experimental and fitted results, respectively.

the intrinsic Au NPs form the TEM image of  $\text{TiO}_2$ -Au NTs (Fig. 1c). Then the as-grown nanotube arrays are removed through an ultrasonication process, leaving the highly-ordered hexagonal concaves imprints on the surface of the Ti-Au alloy sheet, as shown in Scheme S1 and Fig. S4. These hexagonal concaves are also with an average diameter of 150 nm and a wall thickness of 30 nm, similar to that of  $\text{TiO}_2$ -Au NTs.

The Ti-Au alloy foil with these hexagonal concaves imprints is then subjected to the second anodization to yield uniform nanotubes with unique hierarchical nanostructure, avoiding random growth of the nanotubes [25]. In the course of optimizing the time of the second anodization, we found that the nanostructure formed by 10 min has not been broken and exhibits a highest photocurrent response compared with those by applying 20 and 30 min (Fig. S5). The SEM image of  $\text{TiO}_2$ -Au NTPC photocathodes in a top view (Fig. 1d) shows that the top nanostructure is periodic hexagonal-shaped. While from its SEM image in the side view (Fig. 1e) an obvious hierarchical nanostructure is clearly seen. The length of these nanotubes is about 4  $\mu\text{m}$ . From its high resolution TEM (HRTEM) showed in the inset of Fig. 1f, one can clearly see the intrinsic Au NPs, and the diameter of Au NPs is about 8 nm after the anodization process. Furthermore, the  $\text{TiO}_2$ -Au nanotubes maintain their well-aligned morphology.

After the decoration of  $\text{TiO}_2$ -Au nanotubes using a pulsed electrodeposition process for 15 times, Cu NPs with the diameter of about 15–30 nm disperse uniformly and homogeneously on both inside and outside of the hierarchical nanostructure, as shown in Fig. 1g and h. The original two-dimensional nanostructure of  $\text{TiO}_2$ -Au NTPC is remained, leading to no impacts on its absorption and utilization of incident light. The HRTEM image of Cu@ $\text{TiO}_2$ -Au NTPC (see Fig. 1i) shows the Cu structure with the inner-spacing of 0.183 nm and Au structure with the inner-spacing of 0.236 nm, assigned to Cu (200) and Au (111), respectively. These reveal that the deposited Cu NPs are comparatively independent and no alloys structure between Cu NPs and intrinsic Au is formed. Cu NPs and Au NPs are dispersed uniformly and no random agglomeration is seen from the element distribution of Cu@ $\text{TiO}_2$ -Au NTPC (Fig. S6).

The composition analysis of  $\text{TiO}_2$ -Au NTPC before and after depositing Cu NPs was performed. Fig. 2 shows their XPS spectra. For  $\text{TiO}_2$ -Au NTPC, the spectral peaks of Ti 2p, O 1s and Au 4f are observed. The main peaks of Ti 2p are located at 458.4 and

464.0 eV. The interval of 5.6 eV is assigned to  $\text{Ti}^{4+}$  [32]. Two distinctive peaks without any satellite peaks are observed at 86.7 and 83 eV, corresponding to the  $4f_{5/2}$  and  $4f_{7/2}$  spin orbits of  $\text{Au}^0$  [25]. This fact indicates that the noble metal gold is not oxidized during the anodization process. For Cu@ $\text{TiO}_2$ -Au NTPC, the gold peaks are not observed. This might be due to the signal shielding of gold by Cu NPs. The region of Cu 2p consists of Cu 2p<sub>3/2</sub> (932.2, 933.6 eV) and Cu 2p<sub>1/2</sub> (952.0 eV), suggesting the existence of  $\text{Cu}^0$  and very few amounts of  $\text{Cu}^{2+}$  [33]. In addition, the peaks of O 1s are located at 529.8 and 531.1 eV, suggesting the existence of “ $\text{O}^{2-}$ ” ions of the crystalline network of  $\text{TiO}_2$  and the existence of the subsurface of oxygen ions (“ $\text{O}^-$ ”), respectively [34]. A red shift (0.2 eV) and intensity change of O 1s are found in Cu@ $\text{TiO}_2$ -Au NTPC compared with  $\text{TiO}_2$ -Au NTPC, which might be dependent of the nature of the neighbour copper metal.

From the related XRD patterns of  $\text{TiO}_2$  (Fig. S8), the crystal phase of all the  $\text{TiO}_2$  is anatase. This indicates that highly periodic hierarchical structure obtained by a two-step anodization process does not alter the crystal structure of nanomaterials. Note that the diffraction peaks at 35.2°, 38.6°, 40.2°, 53.1° and 63.0° arise from the underlying Ti foil substrate. Au (200) and (111) preferred orientation diffraction peaks appear in the XRD pattern of both  $\text{TiO}_2$ -Au NTPC. This confirms the existence of Au in the NTPCs, in agreement with that observed from its HRTEM image. After the deposition of Cu NPs, the positions of diffraction peaks are mostly consistent compared with diffraction peaks prior to Cu NPs deposition. And Cu (111) preferred orientation diffraction peaks are observed, while Au (111) and Au (200) preferred orientation weak diffraction peak disappears. This is due to the shielding of Au NPs by Cu NPs.

Such a structure of  $\text{TiO}_2$ -Au NTPC is expected to feature its unique absorption characteristics. For example, the appearance of multi-reflection peaks can attribute to the existence of top porous layer in the periodic nanostructure. The nanoporous layer can act as a photonic crystal layer. When light passes through such a highly-ordered nanoporous layer, it is forced or guided to reflect/scatter many times, resulting in an increase in the effective optical path length. In this way, more opportunities are offered for photons to be absorbed by  $\text{TiO}_2$ -Au NTPC and finally higher efficiency for light harvesting is ensured [25]. Together with highly selective and efficient copper electrocatalyst, the Cu@ $\text{TiO}_2$ -Au NTPC photocathode

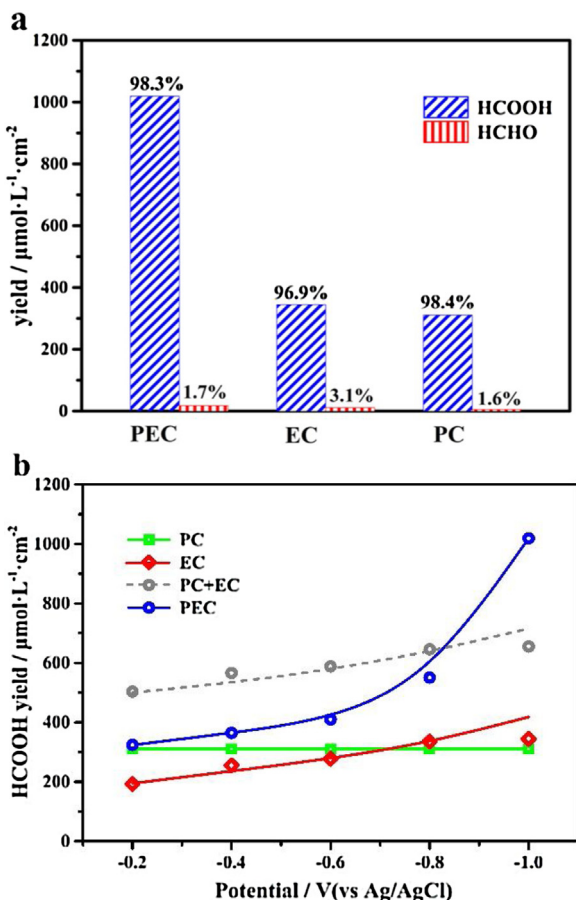


**Fig. 3.** (a) Percentage composition of the reduction products on Cu@TiO<sub>2</sub>-Au NTPC photocathode under PC, EC and PEC condition; (b) the yield ratio of formic acid on Cu@TiO<sub>2</sub>-Au NTPC photocathode under PC, EC, PC + EC, and PEC condition at different applied potential.

is promising for PEC CO<sub>2</sub> reduction using the UV-vis broadband light.

The prepared Cu@TiO<sub>2</sub>-Au NTPC photocathode was then employed for PEC CO<sub>2</sub> reduction in aqueous solution under the simulated solar light irradiation. As control experiments, individual PC CO<sub>2</sub> reduction and EC CO<sub>2</sub> reduction were conducted under similar conditions. Fig. 3a shows some typical results. Whether under PC, EC or PEC condition, the detected reduction products in the liquid phase, were formic acid (>96.9%) and formaldehyde (<3.1%). Other hydrocarbons (e.g., methanol et al.) are not detectable in the liquid phase. In the gas phase, no hydrogen was detected.

The distribution of the main reduction product formic acid at different potentials was further examined through applying PC, EC and PEC. To analyse these results more conveniently, the sum yield ratio of formic acid from sole PC and EC (denoted as PC + EC) was calculated. The related results are shown in Fig. 3b. As the potential increases from -0.2 V to -1.0 V vs Ag/AgCl, the yield ratio of formic acid increases gradually under both EC and PEC conditions. Note that at the applied potential of -0.2 V, the yield ratio of formic acid under the PEC condition is only a little higher than that under the PC condition. A further reduction of the applied potential to -0.8 V, the PEC formic acid's yield ratio approaches more closely to PC + EC. When the applied potential reaches at -1.0 V, the yield ratio of formic acid is up to 1019.3  $\mu\text{mol}\cdot\text{L}^{-1}\cdot\text{cm}^2$ , about 85% higher than that at -0.8 V. Furthermore, the PEC yield ratio of formic acid using PEC has already outnumbered their yield ratios from sole PC and EC. As we can see, in the potential range from -0.2 to -0.6 V, yield ratio of formic acid increases slightly, indicating that the efficiency

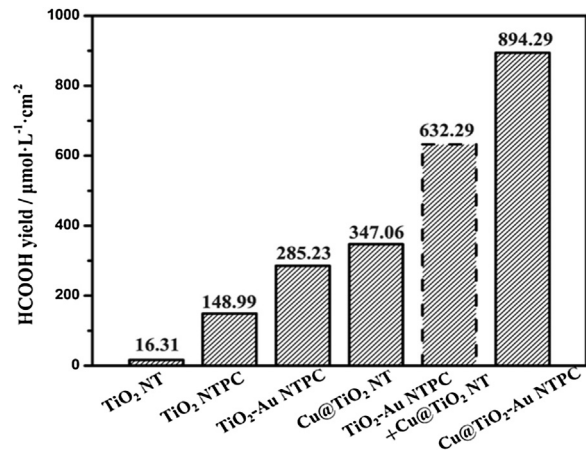


**Fig. 4.** Comparison of the yield ratios of formic acid on TiO<sub>2</sub> NT, TiO<sub>2</sub> NTPC, TiO<sub>2</sub>-Au NTPC, Cu@TiO<sub>2</sub> NT, Cu@TiO<sub>2</sub>-Au NTPC photocathodes under the PEC condition at the applied potential of -1.0 V for 1 h.

of electro-assisted PC is not so significant. From -0.6 to -0.8 V, the effect of electro-assisted PC becomes pronounced, resulting in an obvious promotion of the yield ratio of formic acid. When the potential is up to -1.0 V, the reaction steps into the stage of the PEC integration effect, the highest yield ratio of formic acid is reached. Herein, the Cu@TiO<sub>2</sub>-Au NTPC photocathode we designed exhibits significant advantages for PEC CO<sub>2</sub> reduction in comparison with sole PC or EC. This could be due to a synergistic effect between PC and EC on such a Cu@TiO<sub>2</sub>-Au NTPC photocathode.

The synergistic effect between TiO<sub>2</sub>-Au, NTPC and Cu NPs was then investigated by comparing the yield ratios of formic acid obtained at several different photocathodes at -1.0 V vs. Ag/AgCl for 1 h. As shown in Fig. 4, compared with the yield ratios of formic acid at the TiO<sub>2</sub> NT and TiO<sub>2</sub> NTPC photocathode, the photonic crystal produces 9.13 times more formic acid. For the TiO<sub>2</sub>-Au NTPC photocathode, the yield ratio of formic acid increases nearly by a factor of 91.44% compared with that on the TiO<sub>2</sub> NTPC photocathode without the loading of the intrinsic Au NPs. This result evidences that the Au NPs act as the co-catalyst for PEC CO<sub>2</sub> reduction. As control experiments, PEC CO<sub>2</sub> reduction at the Cu@TiO<sub>2</sub> NT and Cu@TiO<sub>2</sub>-Au NTPC photocathodes were conducted. The yield ratio of formic acid enhances remarkably once Cu NPs are decorated onto the TiO<sub>2</sub> NT and TiO<sub>2</sub>-Au NTPC photocathodes. As for the Cu@TiO<sub>2</sub>-Au NTPC photocathode, its yield ratio is up to 894.29  $\mu\text{mol}\cdot\text{L}^{-1}\cdot\text{cm}^2$  with a Faraday efficiency of 82.6%, nearly 54.83 times that of the TiO<sub>2</sub> NT. Moreover, it is much more than that obtained from sole TiO<sub>2</sub>-Au NTPC and Cu@TiO<sub>2</sub> NT photocathodes. In order to clarify the contribution degrees of each part (photonic crystal, Au NPs and Cu NPs), enhancement factors were further calculated (the detailed calculation please refer to Supporting Information). The enhancement factors are 813%, 91%, and 2028% for photonic crystal, Au NPs, and Cu NPs, respectively. The sum of these numerical values for each part is 632.29  $\mu\text{mol}\cdot\text{L}^{-1}\cdot\text{cm}^2$ , far less than the real yield ratio at the Cu@TiO<sub>2</sub>-Au NTPC photocathode (894.29  $\mu\text{mol}\cdot\text{L}^{-1}\cdot\text{cm}^2$ ). All facts confirm that excellent synergistic effect between Cu NPs and TiO<sub>2</sub>-Au NTPC leads to synergistically promoted PEC CO<sub>2</sub> reduction and effectively controlled generation of formic acid.

To investigate more deeply the functions of each part in the Cu@TiO<sub>2</sub>-Au NTPC photocathode toward PEC CO<sub>2</sub> reduction, the effects of visible light irradiation, electrocatalysts and photonic crystal on the photo-response were examined. Fig. S9 shows the effect of light illumination on the photocurrent density of the TiO<sub>2</sub>-Au NTPC and the Cu@TiO<sub>2</sub>-Au NTPC photocathodes in N<sub>2</sub>-purged 0.1 M Na<sub>2</sub>SO<sub>4</sub> solution. The photocurrent density on the Cu@TiO<sub>2</sub>-

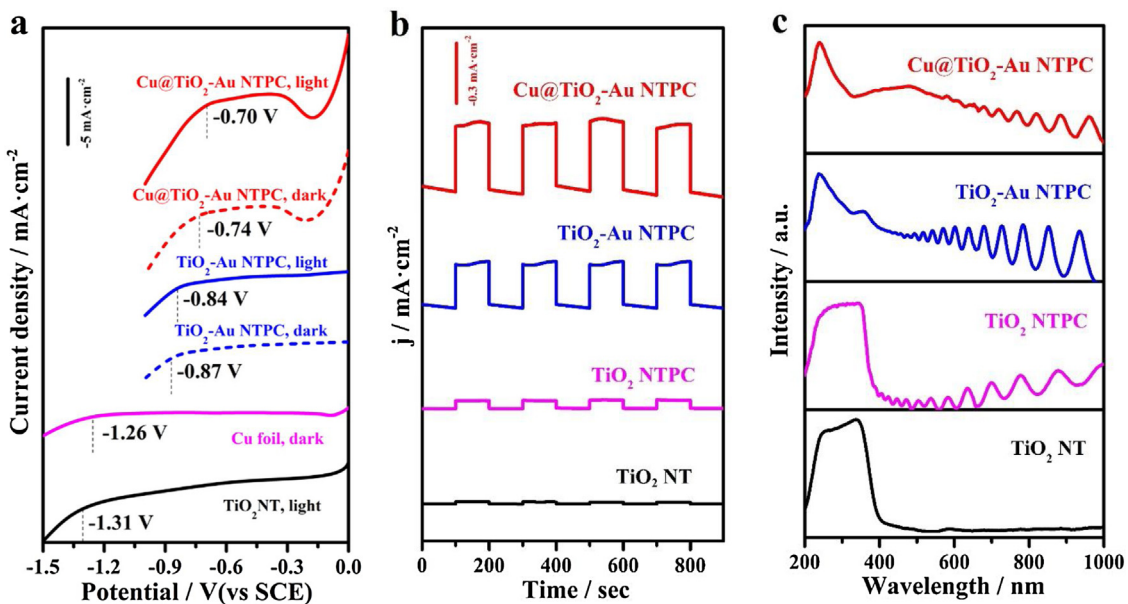


**Fig. 5.** (a) LSVs of Cu@TiO<sub>2</sub>-Au NTPC photocathode (light/dark), TiO<sub>2</sub>-Au NTPC photocathode (light/dark), TiO<sub>2</sub> NT photocathode (light), Cu foil electrode (dark) in CO<sub>2</sub>-saturated 0.1 M Na<sub>2</sub>SO<sub>4</sub> solution; (b) comparison of the amperometric i-t curves for TiO<sub>2</sub> NT, TiO<sub>2</sub> NTPC, TiO<sub>2</sub>-Au NTPC, and Cu@TiO<sub>2</sub>-Au NTPC photocathodes in CO<sub>2</sub>-saturated 0.1 M Na<sub>2</sub>SO<sub>4</sub> solution at -0.7 V under visible-light irradiation; (c) UV-vis diffuse reflection spectra of TiO<sub>2</sub> NT (black), TiO<sub>2</sub> NTPC (pink), TiO<sub>2</sub>-Au NTPC (blue), and Cu@TiO<sub>2</sub>-Au NTPC (red) photocathodes. (For interpretation of the references to colour in this figure legend, the reader is referred to the web version of this article.)

Au NTPC photocathode is obviously higher than that obtained on the TiO<sub>2</sub>-Au NTPC photocathode under light illumination. This is because Cu NPs as a co-catalyst drive effectively the photoelectrons to flow and simultaneously prevent the recombination of electrons and holes. Fig. 5a and Table S1 list the onset potentials on these cathodes in the CO<sub>2</sub>-saturated solution, which were determined by tangent intersection method. The current of CO<sub>2</sub> reduction on a TiO<sub>2</sub>-Au NTPC photocathode increases slightly when the potential is negative than -0.87 V vs. SCE. Once the light illumination is applied, the onset potential shifts to -0.84 V, about 0.47 V more positive than that at a TiO<sub>2</sub> NT photocathode under the light illumination (-1.31 V). After the TiO<sub>2</sub>-Au NTPC photocathode is decorated with Cu NPs, a dramatic enhancement of the current density for EC CO<sub>2</sub> reduction is observed from -0.74 V. This is contributed to the strong activating ability of copper to CO<sub>2</sub> [35]. Such an onset potential is about 0.52 V more positive than that at a copper foil electrode (purity 99.5%), as well as 0.35 V more positive than that at a copper sheet electrode (purity 99.999%) [36]. Furthermore, compared with that on TiO<sub>2</sub>-Au NTPC photocathode, the photocurrent density is nearly doubled at the Cu@TiO<sub>2</sub>-Au NTPC photocathode. These results suggest clearly a favourable PEC performance of a Cu@TiO<sub>2</sub>-Au NTPC photocathode toward CO<sub>2</sub> reduction. Note that in our system the onset potential of PEC CO<sub>2</sub> reduction on the Cu@TiO<sub>2</sub>-Au NTPC photocathode shifts positively 0.04 V under the visible-light irradiation, in accompany with an increase of the current of PEC CO<sub>2</sub> reduction.

The chronoamperometric i-t curves of several photocathodes including TiO<sub>2</sub> NT, TiO<sub>2</sub> NTPC, TiO<sub>2</sub>-Au NTPC and Cu@TiO<sub>2</sub>-Au NTPC were further recorded in the CO<sub>2</sub>-saturated 0.1 M Na<sub>2</sub>SO<sub>4</sub> solution under visible-light irradiation. As shown in Fig. 5b and Table S1, the photocurrent response of TiO<sub>2</sub> NTPC is -0.043 mA cm<sup>-2</sup>, which is obviously enhanced compared with that on the TiO<sub>2</sub> NT photocathode (-0.01 mA cm<sup>-2</sup>). This indicates that photonic crystal layer is conducive to multiple reflection of incident light and then increases the absorption probability, eventually leading to a stronger photocurrent response. As for the TiO<sub>2</sub>-Au NTPC photocathode, its photocurrent response is about -0.22 mA cm<sup>-2</sup>, which enhances greatly in comparison with that on the TiO<sub>2</sub> NTPC photocathode.

This fully verifies the contribution of Au NPs to PEC CO<sub>2</sub> reduction. This is because extraordinary localized SPR properties possessed by Au NPs promote the visible light absorption of the photocathodes [21]. In other words, the electrode's PEC activity is improved by the intrinsic gold doping on the grown TiO<sub>2</sub> NTPC. In order to highlight the advantage of intrinsic Au NPs on TiO<sub>2</sub>-Au NTPC photocathode, Au NPs coated TiO<sub>2</sub> NTs photocathode (Au@TiO<sub>2</sub> NTs) has been fabricated. From the results of the amperometric i-t curves (see Fig. S10), the photocurrent response of Au@TiO<sub>2</sub> NTs is only -0.14 mA cm<sup>-2</sup>, lower than that on the TiO<sub>2</sub>-Au NTPC photocathode. This is due to the well contact between intrinsic Au NPs and TiO<sub>2</sub>. This result indicates that TiO<sub>2</sub>-Au NTPC has higher conductivity and photoelectron-hole separation ability than Au@TiO<sub>2</sub> NTs. Furthermore, the deposition of Cu NPs improves the PEC activity toward CO<sub>2</sub> reduction as well, judging from the better photocurrent response of Cu@TiO<sub>2</sub>-Au NTPC (e.g., -0.36 mA cm<sup>-2</sup> in average), which increases more than 60% of the photocurrent response compared with TiO<sub>2</sub>-Au NTPC. In addition, the photocurrent is stable for a long reaction time. All these results demonstrate the superiority and stability of the Cu@TiO<sub>2</sub>-Au NTPC photocathode for PEC CO<sub>2</sub> reduction.

To check the effect of photonic crystal and the intrinsic Au NPs on the superior PEC ability of the Cu@TiO<sub>2</sub>-Au NTPC photocathode, the optical absorption properties of these photocathodes (TiO<sub>2</sub> NT, TiO<sub>2</sub> NTPC, TiO<sub>2</sub>-Au NTPC, and Cu@TiO<sub>2</sub>-Au NTPC) were measured with UV-vis diffuse reflection spectroscopy (Fig. 5c). The TiO<sub>2</sub> NT only absorbs light in the ultraviolet region of less than 400 nm. The TiO<sub>2</sub> NTPC exhibits not only original UV absorption, but also weak oscillations in the visible region. These are typical interference fringes of highly uniform and periodic thin film structure. For the UV-DRS spectrum of the TiO<sub>2</sub>-Au NTPC photocathode, several strong oscillations are obviously seen with a significant visible absorption enhancement, due to the localized SPR sensitization effect of the Au NPs. In other words, TiO<sub>2</sub>-Au NTPC photocathode expands its absorption region to visible light, which significantly enhances the light absorption of electrode. The slight reduction of the absorption intensity in the ultraviolet region after the decoration of TiO<sub>2</sub>-Au NTPC with Cu NPs is presumably due to a less

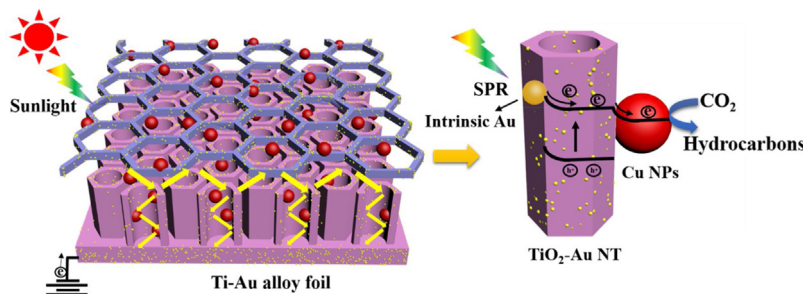


**Fig. 6.** Schematic diagram for the synergy of the photonic crystal, Au NPs, and Cu NPs for  $\text{CO}_2$  reduction under light illumination. The right panel is the energy diagram of the composite photocathode and the mechanism of PEC  $\text{CO}_2$  reduction.

penetration for the incident light into the  $\text{TiO}_2$ -Au NTPC framework. While the enhanced adsorption intensity in the visible region from 400 to 600 nm is probably attributed to the LSPR effect of Cu NPs [4,37]. And the featured oscillations peaks of highly uniform and periodic thin film structure are clearly noticed in the diffuse reflection spectroscopy of the  $\text{Cu}@\text{TiO}_2$ -Au NTPC photocathode. This indicates that the decoration of Cu NPs does not alter the highly uniform and periodic structure. All these data reveal the root of the enhancement of optical absorption and promotion of PEC activity. The unique absorption characteristic of the  $\text{Cu}@\text{TiO}_2$ -Au NTPC photocathode provides a forceful guarantee to achieve synergistic PEC  $\text{CO}_2$  reduction in the UV-vis wide spectral range.

Fig. 6 shows a schematic of the proposed mechanism for the multi-functional synergistic action of the photonic crystal layer, Au NPs, and Cu NPs for  $\text{CO}_2$  reduction under light illumination. Schematically, the incident light is multi-reflected in the  $\text{TiO}_2$ -Au NTPC under light illumination. Surface plasmons that are photo-excited in the Au NPs decay into hot electron–hole pairs, and the hot electrons transiently transfer from the conduction band of Au to the conduction band of  $\text{TiO}_2$  [25,38]. These hot electrons are then through the Schottky barriers at the interface between  $\text{TiO}_2$  and Cu NPs, as well as the photoexcited electrons from  $\text{TiO}_2$ . Lastly, the  $\text{CO}_2$  reduction reaction occurs at the electrocatalyst Cu NPs. Cu is known to be unique in its ability toward  $\text{CO}_2$  reduction, e.g. the products distribution dependent of the applied potentials [36,39]. At the potentials less than  $-0.5$  V vs. NHE, only CO and  $\text{HCOO}^-$  were produced from  $\text{CO}_2$  reduction at a Cu electrode [40,41]. The selectivity toward CO or  $\text{HCOOH}$  depends on the stability of some important reaction intermediates, such as  $^*\text{CO}_2$ ,  $^*\text{CO}$ ,  $^*\text{OCHO}$  and  $^*\text{HCOOH}$  ( $^*$  denotes activated state). Moreover, the work function of Cu is lower than the Fermi level of  $\text{TiO}_2$  [29]. When they are in contact, free electrons flow from Cu to  $\text{TiO}_2$  NTs. Accordingly, Cu NPs are positively charged, which makes the adsorption of  $\text{CO}_2$  on Cu NPs in the form of O–Cu. The suspending carbon atom of chemisorbed  $\text{CO}_2$  then attracts a proton from the solution, leading to chemisorbed  $\text{HCOO}_{\text{ads}}\cdot$ . In addition, the DFT calculation has shown that the formation of a stable intermediate,  $^*\text{OCHO}$ , is favourable to generate  $\text{HCOO}^-$  [41]. Namely, enhanced and selective PEC  $\text{CO}_2$  reduction to formate is achieved on such a multi-functional synergic catalytic interface.

#### 4. Conclusions

A multi-functional synergistic PEC interface, copper nanoparticles and intrinsic Au decorated  $\text{TiO}_2$  nanotube photonic crystal photocathode, has been fabricated on the Ti-Au alloy foil by a facile two-step anodization process together with an electrodeposition process. Such a photocathode effectively combines multiple functions into one, such as the extraordinary localized SPR property of Au NPs, outstanding photocatalytic property of  $\text{TiO}_2$ -Au NTs, excellent electrocatalytic property of Cu NPs and the unique

periodic structure of photonic crystals. Therefore it features superior PEC activity toward  $\text{CO}_2$  conversion. At an applied potential of  $-1.0$  V vs. Ag/AgCl under simulated sunlight illumination, the selectivity of formic acid reaches 98% and the related Faraday efficiency is 82.6%. Such a superior performance has been attributed to the multi-functional synergistic effect between the compositions of  $\text{Cu}@\text{TiO}_2$ -Au NTPC:  $\text{TiO}_2$  PC, Au and Cu nanostructures. For example, the  $\text{TiO}_2$  PC layer acts as a light harvesting fragment, but also provides a carrier larger specific surface area to load gold and copper nanoparticles [42]. The intrinsic Au NPs exhibit the localized SPR sensitization properties that facilitate the optical absorption in the visible region [43]. As for the Cu NPs, they mainly exert electrocatalytic effect to synergistically promote  $\text{CO}_2$  reduction with  $\text{TiO}_2$ -Au NTPC. A surface band bending in the semiconductor induced by Cu NPs helps the electron–hole separation. In summary, this work provides a new approach and photocathode design for  $\text{CO}_2$  transforming to high-value fuels by use of solar energy under mild conditions in the environmental and catalytic field. Future researches focusing on the effect of size, shape, and crystalline structures of these nano-compositions will push photoelectrocatalytic  $\text{CO}_2$  conversion closer to industries.

#### Acknowledgments

This work was financially supported by the National Natural Science Foundation of China NSFC under the projects 21477085 and 21537003 (G.Z.) and by the German Research Foundation (DFG) under project YA344/1-1 (N.Y.).

#### Appendix A. Supplementary data

Supplementary data associated with this article can be found, in the online version, at <http://dx.doi.org/10.1016/j.apcatb.2017.07.029>.

#### References

- [1] A.M. Appel, J.E. Bercaw, A.B. Bocarsly, H. Dobbek, D.L. DuBois, M. Dupuis, J.G. Ferry, E. Fujita, R. Hille, P.J.A. Kenis, C.A. Kerfeld, R.H. Morris, C.H.F. Peden, A.R. Portis, S.W. Ragsdale, T.B. Rauchfuss, J.N.H. Reek, L.C. Seefeldt, R.K. Thauer, G.L. Waldrop, *Chem. Rev.* 113 (2013) 6621–6658.
- [2] M. Cokoja, C. Bruckmeier, B. Rieger, W.A. Herrmann, F.E. Kuehn, *Angew. Chem. Int. Ed.* 50 (2011) 8510–8537.
- [3] Y. Bai, L.Q. Ye, L. Wang, X. Shi, P.Q. Wang, W. Bai, *Environ. Sci. Nano* 3 (2016) 902–909.
- [4] Q. Shen, Z.F. Chen, X.F. Huang, M.C. Liu, G.H. Zhao, *Environ. Sci. Technol.* 49 (2015) 5828–5835.
- [5] C.H. An, J.Z. Wang, W. Jiang, M.Y. Zhang, X.J. Ming, S.T. Wang, Q.H. Zhang, *Nanoscale* 4 (2012) 5646–5650.
- [6] Q. Liu, D. Wu, H.B. Su, R. Wang, C.F. Zhang, S.C. Yan, M. Xiao, Z.G. Zou, *ACS Appl. Mater. Interfaces* 6 (2014) 2356–2361.
- [7] B.Z. Fang, A. Bonakdarpour, K. Reilly, Y.L. Xing, F. Taghipour, D.P. Wilkinson, *ACS Appl. Mater. Interfaces* 6 (2014) 15488–15498.
- [8] Q. Shen, X.F. Huang, J.B. Liu, C.Y. Guo, G.H. Zhao, *Appl. Catal. B-Environ.* 201 (2017) 70–76.

- [9] X.F. Huang, Q. Shen, J.B. Liu, N.J. Yang, G.H. Zhao, *Energy Environ. Sci.* 9 (2016) 3161–3171.
- [10] X.X. Chang, T. Wang, J.L. Gong, *Energy Environ. Sci.* 9 (2016) 2177–2196.
- [11] T. Inoue, A. Fujishima, S. Konishi, K. Honda, *Nature* 277 (1979) 637–638.
- [12] H. Park, H. Kim, G. Mon, W. Choi, *Energy Environ. Sci.* 9 (2015) 411–433.
- [13] Y.L. Li, Y.Y. Bian, H.X. Qin, Y.X. Zhang, Z.F. Bian, *Appl. Catal. B-Environ.* 206 (2017) 293–299.
- [14] C. Tang, L.F. Liu, Y.L. Li, Z.F. Bian, *Appl. Catal. B-Environ.* 201 (2017) 41–47.
- [15] H.X. Qin, Y.Y. Bian, Y.X. Zhang, L.F. Liu, Z.F. Bian, *Chin. J. Chem.* 35 (2017) 203–208.
- [16] F.L. Cao, Y.L. Li, C. Tang, X.F. Qian, Z.F. Bian, *Res. Chem. Intermed.* 42 (2016) 5975–5981.
- [17] Z.F. Bian, J. Zhu, H.X. Li, *J. Photochem. Photobiol. C* 28 (2016) 72–86.
- [18] Y.J. Ji, K.C. Lin, H.G. Zheng, J.J. Zhu, A.C.S. Samia, *Electrochem. Commun.* 13 (2011) 1013–1015.
- [19] Y.N. Zhang, W.N. Huang, Y.J. Zhang, B. Tang, H.S. Xiao, G.H. Zhao, *Mater. Lett.* 168 (2016) 24–27.
- [20] Z.H. Zhang, L.B. Zhang, M.N. Hedihi, H.N. Zhang, P. Wang, *Nano Lett.* 13 (2013) 14–20.
- [21] E. Hutter, J.H. Fendler, *Adv. Mater.* 16 (2004) 1685–1706.
- [22] T. Ohno, T. Higo, N. Murakami, H. Saito, Q.T. Zhang, Y. Yang, T. Tsubota, *Appl. Catal. B-Environ.* 152 (2014) 309–316.
- [23] W.B. Hou, W.H. Hung, P. Pavaskar, A. Goeppert, M. Aykol, S.B. Cronin, *ACS Catal.* 1 (2011) 929–936.
- [24] B.H. Wu, D.Y. Liu, S. Mubeen, T.T. Chuong, M. Moskovits, G.D. Stucky, *J. Am. Chem. Soc.* 138 (2016) 1114–1117.
- [25] K. Lee, R. Hahn, M. Altomare, E. Sellie, P. Schmuki, *Adv. Mater.* 25 (2013) 6133–6137.
- [26] W.G. Tu, Y. Zhou, Z.G. Zou, *Adv. Mater.* 26 (2014) 4607–4626.
- [27] E.E. Benson, C.P. Kubiak, A.J. Sathrum, J.M. Smieja, *Chem. Soc. Rev.* 38 (2009) 89–99.
- [28] K. Manthiram, B.J. Beberwyck, A.P. Aivisatos, *J. Am. Chem. Soc.* 136 (2014) 13319–13325.
- [29] N. Liu, K. Lee, P. Schmuki, *Angew. Chem. Int. Ed.* 52 (2013) 12381–12384.
- [30] J. Hong, W. Zhang, J. Ren, R. Xu, *Anal. Methods* 5 (2013) 1086–1097.
- [31] X.F. Huang, T.C. Cao, M.C. Liu, G.H. Zhao, *J. Phys. Chem. C* 117 (2013) 26432–26440.
- [32] J.C. Yu, L.Z. Zhang, Z. Zheng, J.C. Zhao, *Chem. Mater.* 15 (2003) 2280–2286.
- [33] S.N. Jeng, C.C. Wan, Y.Y. Wang, *J. Electroanal. Chem.* 609 (2007) 68–74.
- [34] D. Jean-Charles, G. Danielle, V. Philippe, L. Alain, *Phys. Chem. Chem. Phys.* 2 (2000) 1319–1324.
- [35] M. Gattrell, N. Gupta, A.A. Co, *J. Electroanal. Chem.* 594 (2006) 1–19.
- [36] Y. Hori, A. Murata, R. Takahashi, *J. Chem. Soc. Faraday Trans.* 85 (1989) 2309–2326.
- [37] G.Y. Jia, J. Wang, L.H. Zhang, H.X. Liu, R. Xu, C.L. Liu, *Europhys. Lett.* 101 (2013) 57005–57009.
- [38] X. Zhang, Y. Liu, S.T. Lee, S. Yang, Z.H. Kang, *Energ. Environ. Sci.* 7 (2014) 1409–1419.
- [39] H. Noda, S. Ikeda, A. Yamamoto, H. Einaga, K. Ito, *Bull. Chem. Soc. Jpn.* 68 (1995) 1889–1895.
- [40] Y. Hori, H. Wakebe, T. Tsukamoto, O. Koga, *Electrochim. Acta* 39 (1994) 1833–1839.
- [41] Z.F. Chen, P. Kang, M.T. Zhang, B.R. Stoner, T.J. Meyer, *Energy Environ. Sci.* 6 (2013) 813–817.
- [42] I. Paramasivam, H. Jha, N. Liu, P. Schmuki, *Small* 8 (2012) 3073–3103.
- [43] W. Hou, S.B. Cronin, *Adv. Funct. Mater.* 23 (2013) 1612–1619.